INORGANIC CHEMISTRY
FRONTIERS

CHINESE CHEMICAL SOCIETY
ROYAL SOCIETY OF CHEMISTRY

RESEARCH ARTICLE

View Article Online
View Journal

Check for updates

Cite this: DOI: 10.1039/d6qi00253f

Marrying V_5S_8 and Sb_2S_3 for volume-tolerant and high-rate potassium-ion storage

Yulian Dong,[a,b] Yubin Fu,[c,d] Vincent Hartmann,[b] Changfan Xu,[b] Ping Hong,[b] Yueliang Li,[e] Huaping Zhao,[b] Weidong Shi,*[a] Ute Kaiser*[e] and Yong Lei*[b]

Received 3rd February 2026,
Accepted 16th April 2026

DOI: 10.1039/d6qi00253f

rsc.li/frontiers-inorganic

To address the challenges of sluggish ion transport and severe volume fluctuation in potassium-ion batteries (PIBs) arising from the large K^+ radius, we design a covalently bonded V_5S_8/Sb_2S_3 heterostructure encapsulated in N-doped carbon (V_5S_8/Sb_2S_3@NC). Calculations using density functional theory (DFT) show that the metallic V_5S_8 and semiconducting Sb_2S_3 form a bandgap-free interface, facilitating rapid charge transfer, while the V–S–Sb covalent bonds enhance interfacial stability. Where V_5S_8 undergoes partial (de)intercalation-induced amorphization that relaxes lattice stress and buffers the ~300% volume expansion of Sb_2S_3 to only ~112% (verified by *in situ* optical microscopy). The synergistic design delivers a high reversible capacity of 657.6 mA h g^{-1} at 0.05 A g^{-1}, long-term cycling stability with 301.5 mA h g^{-1} retained after 600 cycles at 1 A g^{-1}, and rate capability superior to most reported PIB anodes. This work highlights the critical role of covalent interface engineering and amorphization-regulated K^+ storage for high-energy PIB anodes.

1. Introduction

The pursuit of high-performance potassium-ion batteries (PIBs) has driven extensive research into advanced electrode materials that combine high electronic conductivity with structural stability.[1,2] Although the natural abundance and low cost of K supplies make PIBs particularly appealing, they are hindered by the large ionic radius of K^+, which causes sluggish reaction kinetics and severe electrode volume fluctuations.[3–5] Among various anode materials, Sb_2S_3 is a narrow-bandgap semiconductor and has a high theoretical capacity (974 mA h g^{-1}),[6,7] but it suffers from poor electronic conductivity and drastic volume expansion (~300%) upon cycling.[8–10] Conversely, V_5S_8 with zero bandgap (E_g = 0 eV), exhibits exceptional electrical conductivity and high pseudocapacitive storage, but provides limited capacity.[11] A rational integration of these two materials could potentially combine their respective advantages, if the interfacial coupling is sufficiently robust.

Traditional heterostructures often rely on weak van der Waals or electrostatic interactions at the interface, which are insufficient to sustain long-term cycling stability.[12–15] Covalently bonded heterointerfaces can act as atomic-scale "bridges", effectively ensuring strong electronic coupling and structural integrity.[16–18] Here, we propose a covalent heterointerface engineering strategy for K^+ storage. Guided by density functional theory (DFT) calculations, we design a covalently bonded V_5S_8/Sb_2S_3 heterostructure (encapsulated in N-doped carbon, denoted V_5S_8/Sb_2S_3@NC), where V–S–Sb covalent bonds create a bandgap-free interface for rapid charge transfer. DFT simulations indicate the elimination of the bandgap near the Fermi level in the V_5S_8/Sb_2S_3, forming a continuous charge transport channel that greatly improves electronic conductivity.

Theoretical calculations reveal substantial charge transfer from V_5S_8 to Sb_2S_3, generating an internal electric field (IEF) that optimizes charge redistribution and enhances electron mobility.[19–21] As a result, the V_5S_8/Sb_2S_3@NC anode material delivers exceptional performance in half-/full-cell PIBs, including a high capacity (484.7 mA h g^{-1} at 0.1 A g^{-1}) and outstanding rate capability (301.5 mA h g^{-1} at 1 A g^{-1} after 600 cycles). *Ex-situ* XRD, HRTEM, and DFT calculations collectively reveal that the synergistic interaction between the heterostructure and carbon matrix accelerates K^+ migration. It also mitigates volume expansion (only ~112%) and ensures long-term structural integrity of the active material during repeat charging and discharging. This work highlights the critical importance of integrating interfacial covalent bonding with amorphization-regulated ion storage for next-generation PIB anodes.

---

[a] *College of Environmental and Chemical Engineering, Jiangsu University of Science and Technology, Zhenjiang 212003, China. E-mail: swd1978@ujs.edu.cn*
[b] *Fachgebiet Angewandte Nanophysik, Institut für Physik & IMN MacroNano, Technische Universität Ilmenau, 98693 Ilmenau, Germany. E-mail: yong.lei@tu-ilmenau.de*
[c] *School of Energy and Environment, Southeast University, Nanjing, 211189 Jiangsu, China*
[d] *Center for Advancing Electronics Dresden (cfaed) & Faculty of Chemistry and Food Chemistry, Technische Universität Dresden, 01062 Dresden, Germany*
[e] *Central Facility for Electron Microscopy, Electron Microscopy Group of Materials Science, Ulm University, Ulm, 89081, Germany. E-mail: ute.kaiser@uni-ulm.de*

2. Materials and methods

2.1. Preparation of active materials

First, a pale-yellow solution A was formed by swirling and slowly heating 30 ml of deionised (DI) water to 60 °C to dissolve 3 mmol of NH_4VO_3. Solution B was prepared by thoroughly dissolving 15 mmol of C_2H_5NS in 30 mL of ethylene glycol (EG). Following a period of stirring for 0.5 hours, solution B was gradually introduced into solution A under mild agitation for 2 minutes. The combined solution was subsequently enclosed in Teflon-lined stainless-steel autoclave (TLSSA) and then subjected to hydrothermal treatment at 160 °C for a duration of 24 hours. The final product underwent multiple washes, subsequent to an overnight drying to yield the compound known as VS_x.

Initially, 1 mmol of $SbCl_3$ was solved in 30 ml of DI water under moderate stirring to produce solution A. Meanwhile, 3 mmol of C_2H_5NS was dissolved into 30 ml of EG, yielding a clear solution B. After stirring for 0.5 hours, solution B was introduced dropwise to solution A as well as mixed for 2 minutes. The homogeneous mixture was TLSSA-heated at 160 °C for 24 hours. The final product underwent multiple washes with DI water and ethanol through centrifugation, subsequently undergoing overnight drying, to obtain Sb_2S_3.

For the composite VS_x/Sb_2S_3 precursor synthesis, a method analogous to the above was followed. Solution A was prepared by dissolving NH_4VO_3 and $SbCl_3$ in deionized water with stirring and heating, using molar ratios of 3 : 1, 1 : 1, and 1 : 3, respectively. While stirring, solution B, which consists of C_2H_5NS in EG, was carefully introduced to solution A. The solution was warmed to 160 °C for a duration of 24 hours in a TLSSA. After synthesis, the product was washed with 1 : 1 ethanol–water and dried overnight at 100 °C.

To synthesize the N-doped carbon-coated active materials, 100 mg of each precursor (VS_x/Sb_2S_3, Sb_2S_3, and VS_x) and was distributed in 100 ml of Tris buffer (10 mM and pH 8.5) under vigorous stirring for 2 minutes. Ultrasonic treatment for 20 minutes ensured consistent dispersion of the solution. Ultrasonication for 5 minutes followed the administration of 100 mg dopamine hydrochloride. The amalgamation was allowed to agitate gently for 7 hours. The obtained materials were rinsed, dried overnight at 100 °C, and then annealed for 3 hours at 600 °C at 5 °C min^{-1} in a nitrogen environment. The three final active material (V_5S_8/Sb_2S_3@NC, Sb_2S_3@NC, and V_5S_8@NC) were achieved.

2.2. Synthesis of cathode material

The cathode precursor, 3,4,9,10-perylene–tetracarboxylicacid–dianhydride (PTCDA), was thermally treated at 600 °C for a duration of 3 hours in an inert nitrogen environment, at a rate of 5 °C per minute. The resultant carbonized product, named as annealed carbon (AC), exhibited a color transition from dark red to black during pyrolysis. Each batch utilized approximately 300 mg of PTCDA, yielding between 200 to 240 mg of AC.

2.3. Assembly of full cell

The cathode electrode for full-cell testing was combined with AC, Super P conductive carbon, together with CMC binder in a 7 : 2 : 1 mass ratio. AC material had a mass loading of around 4 mg cm^{-2}, while the V_5S_8/Sb_2S_3@NC electrode mass loading was about 1 mg cm^{-2}. Prior to full cell assembly, the AC cathode underwent 5 preconditioning cycles (voltage: 1.5–3.5 V). The anode, derived from V_5S_8/Sb_2S_3@NC, was subjected to pre-potassiation by cycling 5 times from 0.01 V to 3 V, with the final state at 0.01 V. The active material mass in both electrodes and an operating voltage range of 0.5–3.4 V were used for determining capacity.

2.4. Sample characterization, electrochemical measurements, and theoretical calculation

Further details and additional information can be found in the SI.

3. Results and discussion

3.1. Design of V_5S_8/Sb_2S_3@NC and its characterization

The V_5S_8/Sb_2S_3@NC composite was synthesized, as schematically illustrated in Fig. 1a. To begin, $SbCl_3$ and NH_4VO_3 were dispersed in DI water. Then, ethylene glycol containing thio-

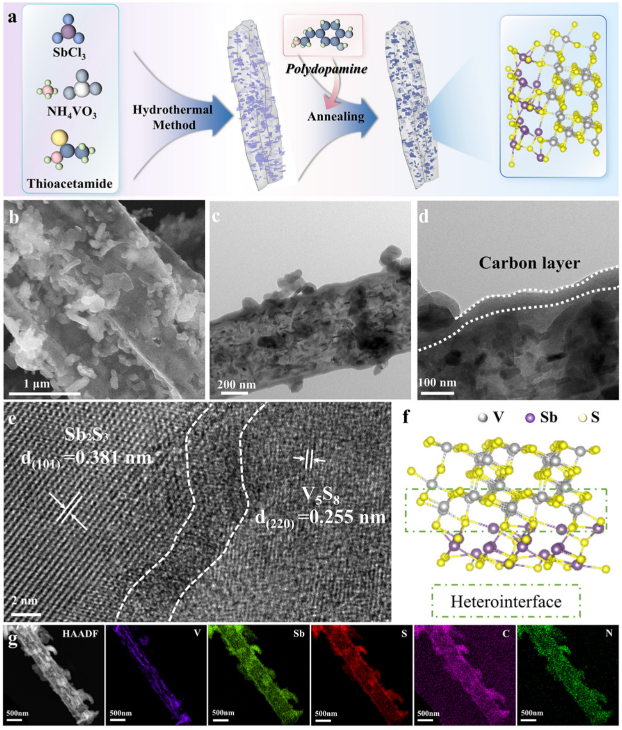

Fig. 1 (a) Conceptual diagram illustrating the synthetic route for the V_5S_8/Sb_2S_3@NC material. (b) SEM image of V_5S_8/Sb_2S_3@NC. (c–e) TEM and HRTEM images depicting the detailed nanostructure of V_5S_8/Sb_2S_3@NC. (f) Atomic ball-and-stick model of the $V_5S_8(110)/Sb_2S_3(101)$ heterointerface. (g) HADDF-EDS analysis of V_5S_8/Sb_2S_3@NC material, confirming the spatial distribution of V, Sb, S, C, and N elements.

acetamide was added. Active material was created from mixed solution by hydrothermal reaction, dopamine coating, and subsequent annealing. Notably, flake-like V_5S_8 nanocrystallites develop and grow uniformly in the Sb_2S_3 matrix. The exterior surface of Sb_2S_3 develops ultrathin nanoribbons due to *in situ* nucleation. As revealed by SEM in Fig. 1b and S1, these nanoribbons exhibit widths ranging from approximately 200 to 400 nm. Furthermore, V_5S_8 nanoparticles or nanoplatelets with dimensions of 65–140 nm is symmetrically anchored on both sides of the ribbons. For comparative analysis, individual Sb_2S_3@NC and V_5S_8@NC composites were synthesized under similar hydrothermal conditions. According to SEM images (Fig. S2 and S3), V_5S_8@NC forms flower-like nanostructures with 500 to 800 nm in diameter and 45–85 nm in thickness. In contrast, Sb_2S_3@NC is composed of densely packed nanorods, which aggregate into larger structures spanning 1180 to 3500 nm in length, as shown in Fig. S3. These aggregates are significantly bulkier than the ultrathin nanoribbon morphology observed in the V_5S_8/Sb_2S_3@NC hybrid. The amount of produced V_5S_8 is a key factor in controlling the morphology of the heterostructure V_5S_8/Sb_2S_3@NC nanoribbons, which can be easily adjusted by varying the molar ratio of precursor vanadium source and antimony source (Fig. S1, S4, and S5). Combined with the morphological analysis, these results suggest that the optimized nanoribbon structure and more uniform phase distribution at the 1 : 1 ratio (V_5S_8/Sb_2S_3@NC) is beneficial for maintaining structural integrity and facilitating ion transport during cycling (Fig. S6).[22] Therefore, the precursor ratio of 1 : 1 was selected for subsequent studies.

3.2. Microstructure and composition

TEM and HRTEM investigations were conducted to better understand the microstructure, as shown in Fig. 1c–e. The V_5S_8/Sb_2S_3@NC material displays a well-maintained nanostructure, wherein V_5S_8 nanosheets or nanoparticles are intimately integrated with Sb_2S_3, and the entire composite is encapsulated by a uniform amorphous carbon layer approximately 20–35 nm thick. This carbon coating not only enhances reaction kinetics but also provides mechanical stability during cycling. In the HRTEM image (Fig. 1e), distinct lattice fringes corresponding to the Sb_2S_3 (101) and V_5S_8 (220), with interplanar spacings of 3.81 and 2.55 Å, respectively, an interfacial region is observed between the two components.[7,23] Considering the coherent contact between the two phases, together with the XPS shifts and DFT-calculated interfacial charge redistribution, this feature is tentatively attributed to local lattice distortion/disorder and the difference in projected potential across the heterointerface, rather than to a separately identified phase. As depicted in Fig. 1f, the V_5S_8 (110) plane used in the DFT calculations belongs to the same crystal plane family as the V_5S_8 (220). The corresponding ball-and-stick model of the V_5S_8 (110)/Sb_2S_3 (101) interface is displayed. We further characterized the structure and composition of V_5S_8/Sb_2S_3@NC using high-angle annular dark field (HAADF) as well as energy dispersive X-ray spectroscopy (EDS), Fig. 1g. This revealed their hierarchical structure and interconnected V_5S_8 nanosheets/particles with Sb_2S_3, as seen in SEM and TEM images. HAADF-EDS elemental mapping confirmed the combination of S, Sb, V, C, and N, indicating that the material is mainly made up of V_5S_8/Sb_2S_3@NC. Considering the local nature of EDS and the carbon support, this result is semi-quantitative, indicating an Sb_2S_3-dominant structure with surface-dispersed V_5S_8, as shown in Fig. S7.

The XRD pattern, Fig. 2a, for Sb_2S_3@NC and V_5S_8@NC correspond closely to Sb_2S_3 (PDF#42-1393) and V_5S_8 (PDF#29-1381), respectively, confirming the successful synthesis of each benchmark material.[7,24] In the V_5S_8/Sb_2S_3@NC composite, however, V_5S_8 peaks appear markedly weaker than in pristine V_5S_8@NC, indicating that crystal growth of the vanadium sulfide phase is partially suppressed by the simultaneous formation of Sb_2S_3, which can be referred to the XRD spectra of V_5S_8 and Sb_2S_3 with mixed-ratio (Fig. S8). Although the diffraction fingerprint of the Sb_2S_3@NC and V_5S_8/Sb_2S_3@NC is mostly consistent, the (020) and (120) reflections at 15.64° and 17.52° are noticeably attenuated, implying that ultrathin Sb_2S_3 nanoribbons develop when V_5S_8 is present. This structural modulation is further corroborated by the SEM and TEM analyses discussed in a later section. For V_5S_8/Sb_2S_3@NC materials, the Raman spectra, presented in Fig. S9, provide structural information that align the effective building of the heterostructure material. The bands around at 324.7 and 254.5 cm^{-1} relate to the A_{1g} mode of V_5S_8 and also the B_{1g} vibrations of Sb_2S_3, respectively. For the reference phases, V_5S_8@NC displays A_g and A_{1g} bands at 146.5 cm^{-1} and 319.25 cm^{-1}, whereas Sb_2S_3@NC shows sharp Sb–S bending modes (A_g and B_{1g}) at 186.41 cm^{-1} and 251.66 cm^{-1}, verifying the coexistence of both components in the V_5S_8/Sb_2S_3 composite.[24,25] In the higher frequency Raman region (900–1800 cm^{-1}), all three active materials exhibit broad bands near 1342 cm^{-1} (disorder-induced D band) as well as 1562 cm^{-1} (graphitic G band), indicating an existence of amorphous carbon.[4]

The elemental composition as well as surface valence states of the three active material samples were clarified by XPS. Full survey spectra (Fig. S10) reveal C, S, N, V, and Sb signals in the composite, with C 1s and N 1s peaks stemming from the N-doped carbon shell. In the Sb 3d region (Fig. 2b), doublets at 538.8/529.5 eV for Sb_2S_3@NC and V_5S_8/Sb_2S_3@NC correspond to Sb $3d_{3/2}$ as well as Sb $3d_{5/2}$ of Sb^{3+} within Sb_2S_3, whereas features at 537.8/528.4 eV are assigned to metallic Sb (0).[8,25] Importantly, the Sb 3d peaks in V_5S_8/Sb_2S_3@NC exhibit a move of approximately 0.6 eV toward higher binding energy relative to pristine Sb_2S_3@NC, signifying stronger electron transfer and enhanced electronic coupling at the V_5S_8–Sb_2S_3 heterointerface.[26] The lower vanadium oxidation states of V^{2+}/V^{+} accounts for the peaks at 522.5 and 515.2 eV (Fig. 2c). In contrast, the distinctive peaks at 523.4 and 516.1 and eV, which are consistent with earlier research, belong to the V $2P_{1/2}$ together with V $2P_{3/2}$ states of V^{4+}, respectively.[11,27] V 2p binding energies in V_5S_8/Sb_2S_3@NC were 0.3 eV lower than in V_5S_8@NC. Such shifts can be attributed to robust interaction across the heterointerface, signifying the transfer of electron

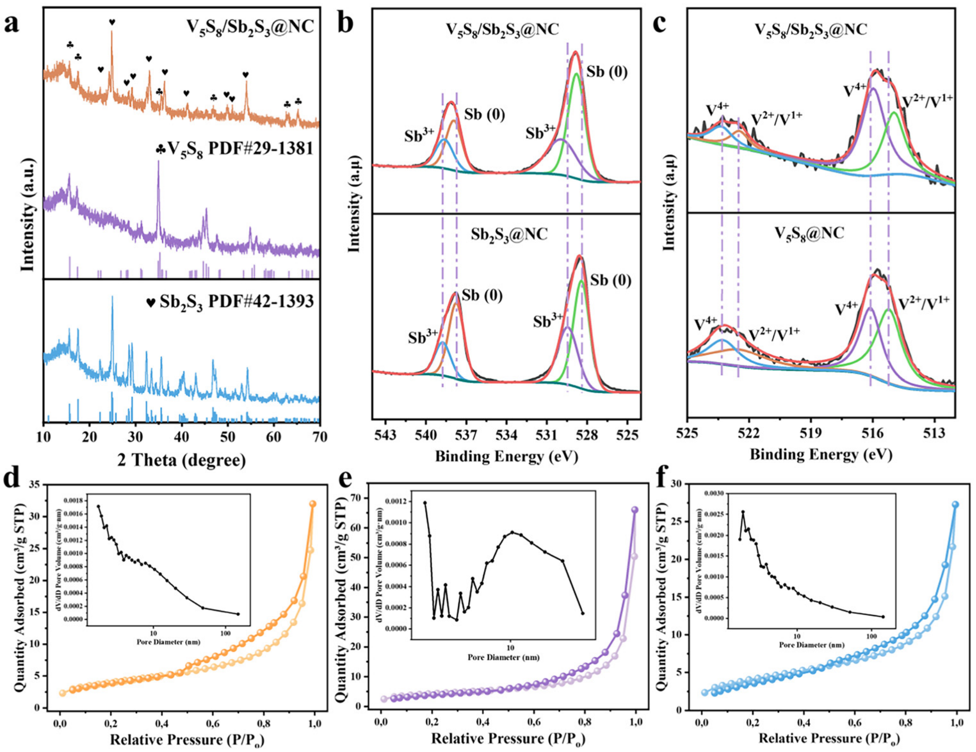

Fig. 2 Structural and chemical characterization for three active materials. (a) XRD patterns. XPS study of: (b) Sb 3d spectra and (c) V 2p spectra. (d–f) Nitrogen adsorption/desorption isotherms were recorded to assess both surface area and porosity; the corresponding pore size distribution is displayed in the insets for each sample (d) V_5S_8/Sb_2S_3@NC, (e) V_5S_8@NC, and (f) Sb_2S_3@NC.

from V_5S_8 to Sb_2S_3.[17,28,29] The total change in binding energy further supports the quick electron transfer and charge separation, which may have been made possible by the powerful IEF.

Nitrogen physisorption analyses (Fig. 2d–f) were used to probe the porosity of the three active material samples. The corresponding pore-size distributions center at approximately 2–9 nm for the V_5S_8/Sb_2S_3@NC composite, about 10 nm for V_5S_8@NC, and 2–4 nm for Sb_2S_3@NC. The broad 2–9 nm interval observed in V_5S_8/Sb_2S_3@NC indicates a hybrid mesoporous framework that likely results from the intergrowth of Sb_2S_3 and V_5S_8 nanocrystals within the N-doped carbon matrix. Brunauer–Emmett–Teller (BET) calculations give a specific surface area of about 15.4 $m^2\ g^{-1}$ for the V_5S_8/Sb_2S_3@NC composite, intermediate between that of Sb_2S_3@NC (14.8 $m^2\ g^{-1}$) and V_5S_8@NC (15.6 $m^2\ g^{-1}$). Such mesopores offer an ample surface area for the electrolyte, reduce K-ion diffusion distance, and facilitate volume swelling, making them helpful to potassiation/depotassiation.[30,31] Thermogravimetric analysis (TGA) was also carried out for V_5S_8/Sb_2S_3@NC and V_5S_8/Sb_2S_3, estimating the carbon content within the composite materials. The initial weight loss below 250 °C may be due to the removal of adsorbed H_2O, as seen in Fig. S11.[32,33] The weight loss observed between 250–500 °C is attributed to the pyrolysis of the carbon, concurrently occurring with the thermal decomposition of V_5S_8 and Sb_2S_3.[34–36] The significant weight loss above 500 °C correlates with accelerated thermal decomposition of V_5S_8 and Sb_2S_3.[37,38] The final residual mass of V_5S_8/Sb_2S_3@NC was approximately 7.1% higher than that of V_5S_8/Sb_2S_3, indicating that N-doped carbon contributed about 7.1 wt% to the V_5S_8/Sb_2S_3@NC composite total mass.

3.3. Electrochemical properties

The electrochemical behavior of the three active material electrodes was investigated using a half-cell potassium system. The first 5 CV curves for the V_5S_8/Sb_2S_3@NC electrode (Fig. 3a) were recorded from 0.01 to 3 V at 0.1 mV s^{-1}. There was one broad peak around 0.9 V and one sharp peak at 0.19 V in the initial cathodic scan, which belonged to the intercalation of K^+ into V_5S_8/Sb_2S_3 and the alloying reaction of Sb, respectively, and accompanied by the formation of solid electrolyte interphase (SEI) film.[7,39] The HRTEM and XRD data can validate this, which will be detailed later. Oxidation peaks around at 0.64 along with 1.26 V may come from step-depotassiation.[8] Electrochemical behavior of Sb_2S_3@NC and V_5S_8@NC materials was compared using CV curves. Fig. S12a illustrates that the initial insertion process of V_5S_8 into $K_xV_5S_8$ accounts for observed reduction in the peak at 0.77 V. The conversion behavior of K^+ and SEI layer generation accounted for the subsequent peaks observed at 0.48 V as well as 0.01 V, respectively.[11] A redox couple observed at 0.67/0.51 V originates from the V-centred conversion reaction. In contrast, the CV trace of the Sb_2S_3@NC electrode (Fig. S10b) reveals two visible redox pairs that reflect successive redox and alloying events during

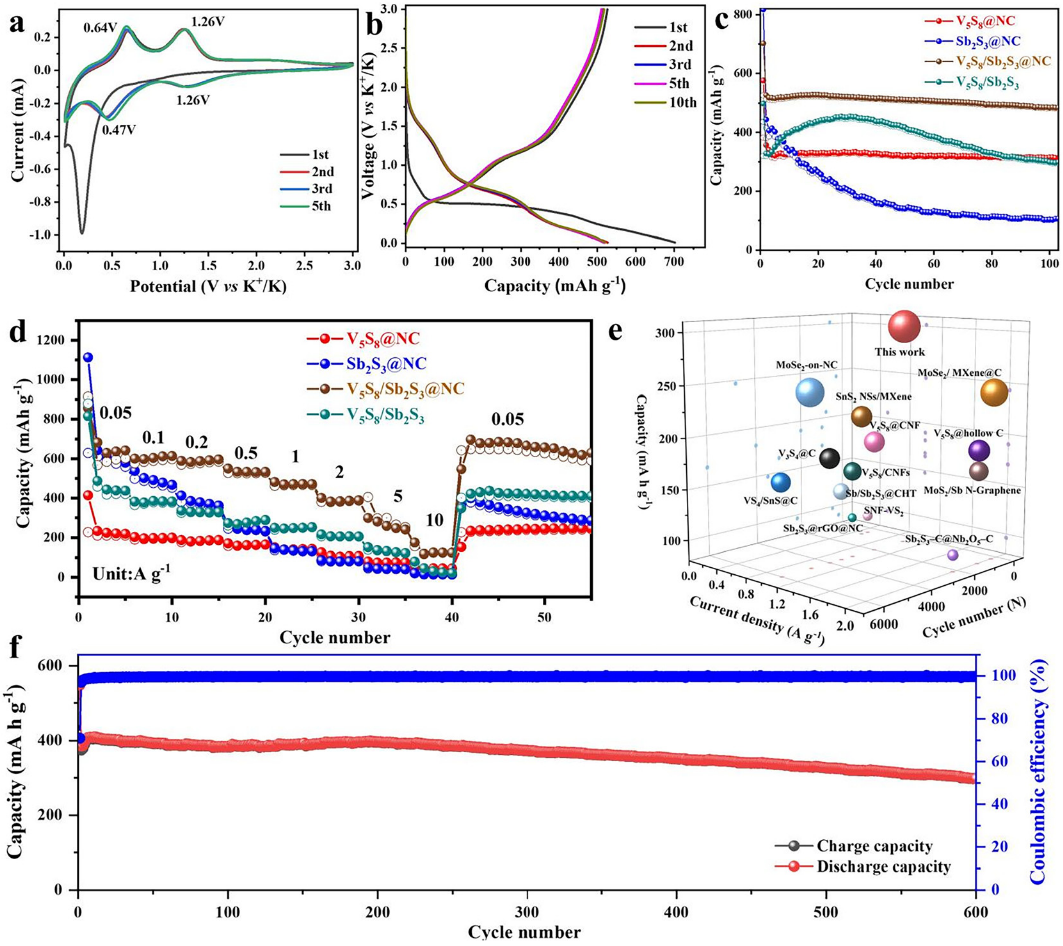

Fig. 3 Electrochemical characteristics of the three active material electrodes. (a) CV curves of V_5S_8/Sb_2S_3@NC at 0.1 mV s^{-1}. (b) GCD profiles of V_5S_8/Sb_2S_3@NC at 0.1 A g^{-1}. (c) Cycling performance at 0.1 A g^{-1}, and (d) rate performance comparison of active material electrodes at different current density. (e) V_5S_8/Sb_2S_3@NC rate performance comparison with published anodes. (f) Extended cycling capacity of V_5S_8/Sb_2S_3@NC at 1 A g^{-1}.

potassiation. The cathodic sweep reveals peaks at approximately 0.76, 0.18, and 0.02 V, indicating multiple Sb and K alloying and SEI film development. The CV curves exhibit near overlap, with peaks at 1.32/1.14 V, revealing K^+ intercalation/extraction in $K_xSb_2S_3$, while sharp signals at 0.42 and 0.64 V arise from reversible alloying and dealloying of K with metallic antimony.[6]

The V_5S_8/Sb_2S_3@NC galvanostatic charge–discharge (GCD) curves recorded over the first 10 cycles are shown in Fig. 3b. With 0.1 A g^{-1} current, V_5S_8/Sb_2S_3@NC attains a 1st-cycle discharge capacity of 702.1 mA h g^{-1} along with an associated charge capacity of 526.3 mA h g^{-1}, yielding an initial coulombic efficiency (CE) of as much as 75%. The inaugural GCD trace exhibits a series of gently sloping potential plateaus, reflecting the multistep electrochemical transformations discussed earlier, consistent with CV observations. By contrast, the initial CE of Sb_2S_3@NC and V_5S_8@NC electrodes were relatively lower, measuring 66% and 53%, respectively, as presented in Fig. S13. As displayed in Fig. 3c, at 0.1 A g^{-1}, V_5S_8/Sb_2S_3@NC electrode sustains a substantial capacity of around 484 mA h g^{-1}, achieving a maximum CE of 99.7%, even at 100th cycle. This capacity is much greater than the capacities of V_5S_8@NC, which is 315 mA h g^{-1}, and Sb_2S_3@NC, which is 103.5 mA h g^{-1}. We also assessed the carbon-free V_5S_8/Sb_2S_3 electrode for comparison in order to further clarify the function of N-doped carbon. Fig. 3c depicts that the electrochemical performance exhibits a distinct trend, with the specific capacity initial increasing from 382.1 mA h g^{-1} at 2nd to 454.8 mA h g^{-1} at 31st cycle, followed by a gradual decline to 300 mA h g^{-1} at 100th cycle. This behavior makes it abundantly evident that the N-doped carbon in the V_5S_8/Sb_2S_3@NC electrode largely serves as a protective layer, greatly increasing structural stability during cycling while making a negligible contribution to the total capacity.

Additionally, the V_5S_8/Sb_2S_3@NC electrode demonstrates outstanding rate performance during the broad current density range, as depicted in Fig. 3d. Specifically, it delivers discharge capacities of around 642, 614, 597, 533, 471, 389, 241, and 124 mA h g^{-1} at the present density of 0.05, 0.1, 0.2, 0.5, 1, 2, 5, and 10 A g^{-1}, respectively. Remarkably, when the current density returns to 0.05 A g^{-1}, the V_5S_8/Sb_2S_3@NC recovers an impressive capacity of around 657 mA h g^{-1}, indicative of its outstanding structural reversibility and superior cycling stability. It is noted that the specific capacity of the $V_5S_8/Sb_2S_3@NC$ electrode returns to 0.05 A g^{-1} at the rate test, which is slightly higher than the initial 5 cycles' capacity (~642 mA h g^{-1}) after the electrode has been activated through low-current cycling (*e.g.*, at 0.1 or 0.2 A g^{-1}). This initial activation helps optimize electrode–electrolyte wetting and improves K^+ diffusion, resulting in an increased observed capacity once the current reaches 1 A g^{-1}.[27,40,41] In contrast, the single-phase sulfide electrodes of $V_5S_8@NC$ and $Sb_2S_3@NC$ experienced a rapid capacity decay, with capacities dropping to 44.7 and 13.4 mA h g^{-1}, respectively, at the high current rate of 10 A g^{-1}. Interestingly, the carbon-free V_5S_8/Sb_2S_3 electrode also shows a similar trend, but exhibits higher specific capacities than both $V_5S_8@NC$ and $Sb_2S_3@NC$ in limited cycles, which highlights the synergistic effect and intrinsic of V_5S_8/Sb_2S_3 heterostructures to enhance K storage performance. The remarkable rate capability of $V_5S_8/Sb_2S_3@NC$ primarily arises from the improved transport of ions and electrons boosted by its heterostructure, where the heterointerface generates a IEF as well as a denser electron cloud, speeding up charge transfer while promoting charge redistribution, as supported by theoretical calculations, which will be discussed in future studies.[11,42,43] Moreover, compared with reported V-based or Sb-based anodes for PIBs, as shown in Fig. 3e and Table S1.[6,8,11,42,44–52] This indicates that $V_5S_8/Sb_2S_3@NC$ exhibits a competitive capacity level and superior capacity retention at high current density. Notably, it achieves a balanced combination of high capacity and long-term cycling stability, whereas most reported systems typically sacrifice one for the other. This balanced performance highlights the advantage of the heterostructure design in simultaneously regulating reaction kinetics and structural stability.

The $V_5S_8/Sb_2S_3@NC$ electrode experienced long-term cycling analysis for its durability at 1.0 A g^{-1} (Fig. 3f), maintaining a discharge capacity exceeding 300 mA h g^{-1} after 600 cycles, with a CE consistently above 99.6%. The specific capacity attained during the rate capability test (~470 mA h g^{-1} at 1 A g^{-1}) surpassed the stabilized capacity (~410 mA h g^{-1}) observed under prolonged cycling at the same current. This difference arises from the gradual structural evolution and interfacial stabilization, while the rate test reflects transient capacity under partially actively involved.[53] For comparison, the $V_5S_8@NC$ electrode demonstrated a lower capacity around 111 mA h g^{-1} (Fig. S14), whereas the $Sb_2S_3@NC$ electrode exhibited an even lower value of 72 mA h g^{-1} (Fig. S15) after 600 cycles. These results indicate that $V_5S_8/Sb_2S_3@NC$ exhibits superior cycling stability compared to both $V_5S_8@NC$ and $Sb_2S_3@NC$, further highlighting its potential as a stable and high-performance electrode material for PIBs.

3.4. Electrochemical performance and kinetic mechanism analysis

To assess the influence of capacitive behavior on electrochemical performance of three active material electrode, CV calculations were conducted. And CV curves for sweep speeds 0.2 to 1.0 mV s^{-1} are shown in Fig. 4a and S16. As the scan rates increased, the curves follow a similar trend with slight peak shifts, indicating a potential decline in cell performance attributed to electrode–electrolyte contact or slow electron transport. The area enclosed by the CV curve reflects the combined effects of faradaic processes and non-faradaic double-layer storage of charges processes. The faradaic process consists of major processes: (i) the intercalation of K^+ ions into the host material, and (ii) a pseudocapacitive reaction related to charge transfer at or near the surface of active particles.[41,54] Scan rate (v) and peak current (i) are related by the formula $i = av^b$, where a and b refer to constants.[8] A value of b = 0.5 indicates a semi-infinite diffusion control reaction, while a value of b = 1 corresponds to a capacitive process. In Fig. 4b, the extracted b-values for the redox peaks Re1 (0.82) along with Re2 (0.87), suggesting that capacitive behavior is the dominant mechanism in $V_5S_8/Sb_2S_3@NC$. For comparison, Fig. S17a reveals that $V_5S_8@NC$ exhibits a b-value approaching 1, reinforcing the dominance of capacitive storage. In contrast, $Sb_2S_3@NC$ shows a b-value below 0.8, as shown in Fig. S17b, suggesting the coexistence of both capacitive and diffusion behavior. Furthermore, a voltammetry sweep rate-dependent ana-

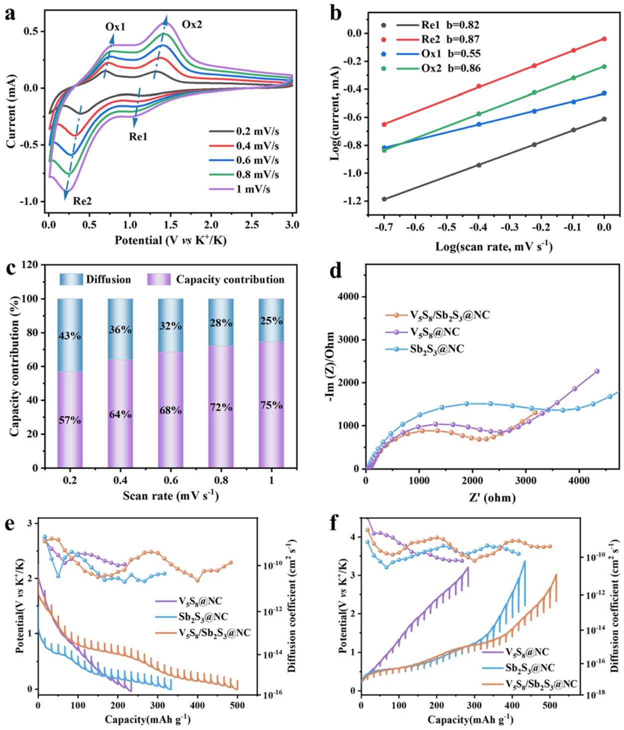

Fig. 4 Electrochemical kinetics and ion transport analysis of $V_5S_8/Sb_2S_3@NC$-based electrodes. (a) CV profiles of the $V_5S_8/Sb_2S_3@NC$ electrode. (b) Log–log charts demonstrating the linear correlation. (c) Proportion of capacitive *versus* diffusion-controlled contributions. (d) EIS of three electrodes ($V_5S_8/Sb_2S_3@NC$, $V_5S_8@NC$, and $Sb_2S_3@NC$) after 100 cycles. GITT profiles during (e) the discharge and (f) the charge processes, along with the corresponding K^+ diffusion coefficients for the three electrodes.

lysis was performed to investigate the specific pseudocapacitive contributions and diffusion-controlled reactions in the V_5S_8/Sb_2S_3@NC electrode, as further elucidated by the equation:

$$i(V) = k_1\nu + k_2\nu^{1/2}. \tag{1}$$

The measured current (i) at a given voltage consists of two primary components: a diffusion-limited contribution (proportional to $k_2\nu^{1/2}$) and a surface-controlled capacitive response (proportional to $k_1\nu$).[8] As illustrated in Fig. 4c, the capacitive behavior of V_5S_8/Sb_2S_3@NC was evaluated across scan rates ranging (0.2–1.0 mV s^{-1}). Notably, the capacitive portion rises from 57% at the lowest scan rate to 75% as the rate increases to 1 mV s^{-1}, indicating a growing dominance of surface-controlled charge storage at higher scan speeds. Fig. S18 shows that at 1 mV s^{-1}, the surface capacitive effect contributes 75% of the V_5S_8/Sb_2S_3@NC electrode's capacitance, identifying it as the main contributor. In comparison, the surface-controlled charge storage behavior exhibited by V_5S_8/Sb_2S_3@NC and V_5S_8@NC was similar to that observed in Sb_2S_3@NC, as shown in Fig. S19. However, V_5S_8@NC consistently delivered a greater pseudocapacitive contribution across all tested scan rates, with values varying between 77% to 88% (scan rates: 0.2–1.0 mV s^{-1}). In contrast, Sb_2S_3@NC demonstrated significantly reduced level of pseudocapacitive contribution, ranging from 25% to 43% over the same scan rate interval. The presence of V_5S_8 facilitates improved reaction kinetics in the V_5S_8/Sb_2S_3@NC electrode. Consequently, capacitive processes dominate at elevated scan rates, supporting V_5S_8/Sb_2S_3@NC's improved rate performance.

Furthermore, in order to assess the impact of the active material structures on the reaction kinetics of K^+, EIS technique was carried out. The Nyquist plots of the tested materials display a characteristic semicircular region followed by an inclined linear segment, as depicted in Fig. 4d. At low frequencies, the diagonal line indicates diffusion, while the semicircle represents high-frequency charge transfer impedance (R_{ct}). Table S2 shows that the R_{ct} value of V_5S_8/Sb_2S_3@NC (1745 Ω) is much lower after 100 cycles compared to the Sb_2S_3@NC (3161 Ω) and V_5S_8@NC (2211 Ω). It is important to highlight that the fresh V_5S_8@NC electrode exhibits a lower R_{ct} of 1062 Ω compared to V_5S_8/Sb_2S_3@NC (1606 Ω) and Sb_2S_3@NC (1747 Ω) which is a good indication that V_5S_8@NC has the best conductivity in agreement with other works.[11] Furthermore, V_5S_8/Sb_2S_3@NC electrode EIS spectra were taken in the fresh state as well as after the 1st, 2nd, 5th, and 50th cycles (Fig. S20). During the first cycle, the V_5S_8/Sb_2S_3@NC shows the highest R_{ct} value of 2022 Ω, which reflects a deceleration in charge transfer likely resulting from the appearance of the SEI layer. Within the first fifty cycles of V_5S_8/Sb_2S_3@NC, the R_{ct} value decreases significantly, which significantly improves the battery conductivity, then the active material is slowly destroyed and the impedance increases. Table S3 shows the whole R_{ct} value and fitting circuit fitting results.

To understand the active electrode's electrochemical kinetics, compare the chemical K^+ diffusion coefficient, where is estimated *via* a simplified Fick's second law:

$$D_k = \frac{4}{\pi\tau}\left(\frac{m_b V_M}{M_B S}\right)^2 \left(\frac{\Delta E_s}{\Delta E_t}\right)^2 \left(t \ll \frac{L^2}{D}\right) \tag{2}$$

where D_k is the K^+ diffusion coefficient ($cm^2\ s^{-1}$), the τ denotes the duration of the applied current (s), m_b is the active electrode material mass (g), M_B corresponds to its molar mass (g mol^{-1}), V_M is its molar volume ($cm^3\ mol^{-1}$), as well as S is its geometric surface area (cm^2). The steady-state voltage variation resulting from the pulse is represented as ΔE_S, ΔE_t indicates the transient potential shift observed during the pulse at constant current. The trends of D_K value for three active material electrodes as illustrated in Fig. 4e and f, exhibit comparability. The diffusion coefficients of K^+, varying with cell voltage, are estimated to range from 1.33×10^{-9} to 2.37×10^{-11} for the discharge process and from 2.4×10^{-9} to 6.48×10^{-11} ($cm^2\ s^{-1}$) charging process in the V_5S_8/Sb_2S_3@NC electrode. Furthermore, a sudden or gradual decline in the diffusion coefficient is noted at specific discharge and charge potentials where the electrochemical mechanism transitions between intercalation, conversion, and alloy reactions. This pattern of one or multiple significant or gradual drops in diffusion rate across discharge and charge potentials is also evident in other two-phase transition metal electrodes.

Ex situ characterizations (*e.g.*, XRD, TEM) were conducted on V_5S_8/Sb_2S_3@NC electrodes to clarify the K^+ storage mechanism and explore changes in structure throughout the charge–discharge processes (Fig. 5 and S21). At 0.6 V (corresponding to terminated state II, Fig. 5a), V_5S_8 is partially transformed into $K_xV_5S_8$. As the electrode continues to discharge to 0.01 V (terminated state III), $K_xV_5S_8$ peaks shift slight to lower angles, implying more potassiation and the production of $K_{x+y}V_5S_8$. The metal V peak is not observed, although K_3Sb is at 0.01 V. During potassiation, no conversion reaction to metal V happened at a potential of 0.01 V, and it is likely that only K was inserted into V_5S_8. As illustrated in Fig. 5b (terminated states IV to VI), K^+ ions were removed from K_3Sb and $K_{x+y}V_5S_8$ during charging, resulting in the simultaneous presence of $K_xV_5S_8$ and a partial restoration of V_5S_8, Sb_2S_3, and amorphous V_5S_8 at 3 V.[55] This remarkable contrast suggests the existence of interfacial contacts between the produced $K_xV_5S_8$, Sb_2S_3, and amorphous V_5S_8 inside the V_5S_8/Sb_2S_3@NC, and that this amorphization is partially irreversible to the initial state of V_5S_8. The *ex situ* HRTEM results provide support for this hypothesis, as illustrated in Fig. 5e–g (discharge state at 0.01 V) and Fig. 5h–j (charge state at 3 V). It is clearly evident that the (101) and (111) planes of $K_xV_5S_8$ and K_2S_2, respectively, are represented by lattice fringes measuring 0.566 and 0.34 nm. Also, black K_3Sb nanocrystals with 0.31 nm lattice edges that are indexed to the (110) plane are observed supporting the XRD spectrum and prior study.[7,51] The presence of a large amorphous region and obvious lattice diffraction stripes corresponding to the (101) plane of Sb_2S_3 (0.385 nm) and the (112) plane of V_5S_8

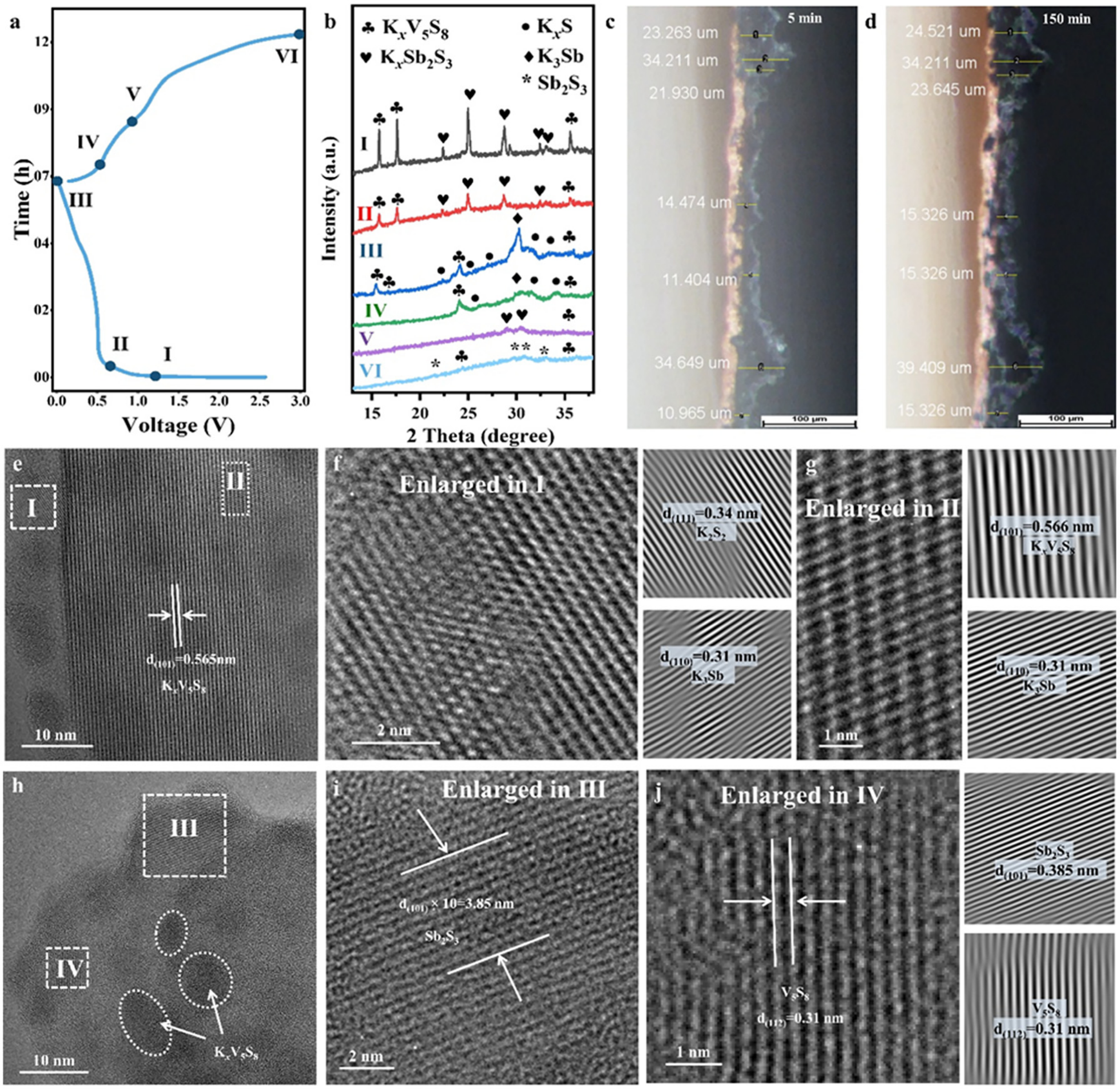

Fig. 5 K^+ storage mechanism of V_5S_8/Sb_2S_3@NC electrode. (a) Voltage–time curve of V_5S_8/Sb_2S_3@NC electrode during the 1st charge–discharge cycle. (b) Selected *ex situ* XRD patterns of V_5S_8/Sb_2S_3@NC electrodes at various states (I–VI). Selected *in situ* optical microscopy images of K potassiation into the V_5S_8/Sb_2S_3@NC electrode after (c) 5 min and (d) and 150 min. TEM images of V_5S_8/Sb_2S_3@NC: (e–g) Discharged to 0.01 V and (h–j) Charged to 3.0 V during the 1st cycle.

(0.31 nm) are evident on charging to 3 V, as seen in Fig. 5h–j. *Ex situ* XRD and HRTEM indicate that V_5S_8 undergoes partial amorphization during the potassiation/depotassiation process, resulting in the coexistence of crystalline and amorphous regions in the cycled electrode, these data consistently indicate that V_5S_8 undergoes partial amorphization and/or nanocrystallization during potassiation/depotassiation. Such structural evolution is expected to improve structural adaptability during cycling. The experimental findings indicate that the K^+ ion storage process in V_5S_8/Sb_2S_3 may be summed up as follows:

Initial potassiation:

$$Sb_2S_3 + xK^+ + xe^- \rightarrow K_xSb_2S_3 \rightarrow 3K_xS + 2Sb$$

and

$$V_5S_8 + xK^+ + xe^- \rightarrow K_xV_5S_8$$

Further potassiation:

$$3K_xS + 2KSb + (3-x)K^+ + (3-x)e^- \rightarrow K_2S_3 + 2K_3Sb$$

and

$$K_xV_5S_8 + yK^+ + ye^- \rightarrow K_{x+y}V_5S_8$$

Depotassiation:

$$2K_3Sb - 6K^+ - 6e^- \rightarrow Sb_2S_3$$

and

$$K_{x+y}V_5S_8 - yK^+ - ye^- \rightarrow K_xV_5S_8.$$

3.5. Analysis of V_5S_8/Sb_2S_3@NC structural stability and morphological evolution after cycling

A direct observational approach has been used to monitor the topological morphology of the V_5S_8/Sb_2S_3@NC electrode in order to investigate its structural integrity and expansion process. As shown in the movie and selected screenshots, *in situ* optical microscope recorded potassiation-induced morphological alterations. Interestingly, after 5 to 150 minutes of potassiation (Fig. 5c and d), a slightly whitish and darkened interface started to appear on the electrode surface, suggesting that the active material potassiated quickly. Movie S1 shows that despite the rapid potassiation, the electrode layer expands at a relatively slow rate that can be neglected. The average electrode expansion rate, as assessed by comparison and measurement of many reference sites, was found to be roughly 112.59%, which is considered competitive compared to the significantly higher volume changes typically observed in alloying and conversion-type electrode materials.[56,57]

Ex situ SEM was also utilized to monitor the morphology evolution of V_5S_8/Sb_2S_3@NC electrode throughout the cycling process. After the first cycle, the electrode surface was uniformly coated with a relatively flat and compact SEI layer, accompanied by the formation of ultrafine particles distributed across the surface (Fig. S22). It's worth noting that electrolyte-engineered interphases (*e.g.*, bandgap-engineered SEI and K_2SO_3-rich interphase) are also a potential factor for improving electrode performance, as has been observed in other material systems.[58–60] This warrants further investigation, but it's not the focus of this work. With continued cycling, these fine particles expanded and gradually fused together, forming a coherent and tightly bound outer layer that encapsulated the V_5S_8/Sb_2S_3@NC (Fig. S23). The creation of a strong SEI that could endure the mechanical stress brought on by repeated potassiation/depotassiation was demonstrated by the electrode's surface becoming more uniform and structurally stable. This structural adaptation likely contributed to the enhanced long-term cycling performance of the electrode. Significant morphological changes were noted after 700 cycles, though, as the outermost layer lost its distinctive granular texture and it became more challenging to discern between the conductive additives, active material, and other structural elements (Fig. S24). This phenomenon may indicate the gradual passivation or structural collapse of the electrode surface, which may be the major cause of electrode material electrochemical activity decline and active material failure.

3.6. DFT calculation

Theoretical DFT simulations were performed to investigate the correlation between the reaction kinetics of V_5S_8, Sb_2S_3, and V_5S_8/Sb_2S_3 heterostructure with K^+ under ideal conditions. Fig. 6a–c illustrate the calculated charge density difference isosurfaces (at an isovalue of 0.007 e Å^{-3}) for V_5S_8, Sb_2S_3, and V_5S_8/Sb_2S_3, respectively. The blue and yellow areas indicate regions of charge depletion and accumulation, respectively, providing a visual indication of electron redistribution. Notably, in the V_5S_8/Sb_2S_3 heterostructure (Fig. 6c), a distinct electron redistribution and charge transfer from V_5S_8 to Sb_2S_3 is observed, highlighting the electronic coupling at the interface and the successful establishment of the heterostructure. The density of states (DOS) plots (Fig. 6d) demonstrate that V_5S_8 displays metallic characteristics, whereas Sb_2S_3 functions as a type of semiconductor along with calculated bandgap of approximately 1.2 eV, in agreement with prior literature.[11,57] Interestingly, the V_5S_8/Sb_2S_3 heterostructure presents a continuous DOS near the Fermi level, indicating the absence of a bandgap and suggesting a substantial enhancement in electrical conductivity. This enhanced conductivity is due to the creation of the heterointerface, which imparts metallic behavior to the V_5S_8/Sb_2S_3 hybrid. When materials possessing different electronic structures form a junction, electron redistribution occurs at the interface, resulting in the emergence of an internal electric field.[19,61,62] This field stimulates the accumulation of K^+ ions in the negative-charge area, effectively acting as an ion reservoir. A concentration gradient is created when the localized region retains a high concentration of potassium

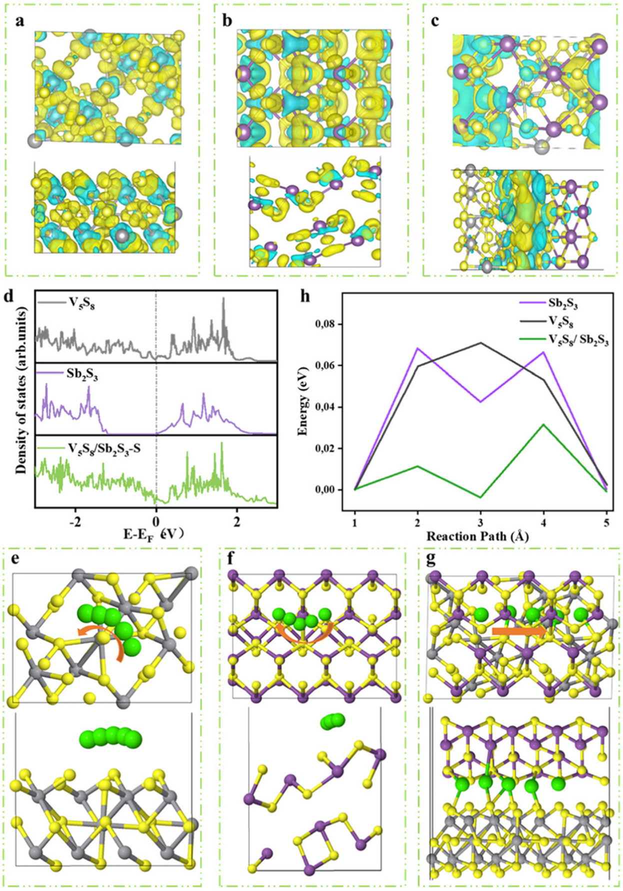

Fig. 6 The differential charge density images of (a) V_5S_8, (b) Sb_2S_3, and (c) V_5S_8/Sb_2S_3 with the top view (up) and side view (down) (yellow: charge increase, blue: charge decrease). (d) The DOS plot of V_5S_8/Sb_2S_3, Sb_2S_3, and V_5S_8. K ion migration paths in the (e) V_5S_8, (f) Sb_2S_3, and (g) V_5S_8/Sb_2S_3 with the view of top (up) and side (down). (h) The kinetic energy curve of K-ions on their diffusion path.

ions even when the IEF weakens as a result of charge equilibrium.[14,63,64] This mechanism promotes efficient charge transfer across the interface, thereby accelerating the overall electrochemical kinetics of the electrode system.

The ion diffusion barrier energies in the bare V_5S_8, bare Sb_2S_3, and V_5S_8/Sb_2S_3 heterostructure were employed to evaluate K-ion migration behavior using the CI-NEB method. Fig. 6e–g illustrates the plausible K-ion diffusion pathways across the three model systems. For the V_5S_8/Sb_2S_3 heterostructure, ion movement is primarily considered within the interlayer region of V_5S_8, due to its external positioning in the composite. Corresponding energy profiles along these migration routes are presented in Fig. 6h. The computed energy barrier for K-ion migration within the V_5S_8/Sb_2S_3 interface is notably low at 0.0314 eV, which is significantly reduced compared to the values for bare V_5S_8 and Sb_2S_3, measured at 0.0596 and 0.0681 eV, respectively. The lower energy barrier increases the transfer of K^+, which can improve the reaction kinetics and charge storage of K in V_5S_8/Sb_2S_3. Combined with the *ex situ* XRD and HRTEM results, which suggest partial amorphization and structural disordering of V_5S_8 during cycling, we infer that the superior electrochemical performance arises from the synergy between heterointerface-enabled fast transport and amorphization-enabled structural adaptability.[65–67] In particular, the partially amorphous V_5S_8 may provide more disordered K-ion diffusion environments and better accommodate stress evolution, which is consistent with the fast diffusion kinetics from GITT and the stable long-term cycling behavior.[67]

3.7. Electrochemical performance of V_5S_8/Sb_2S_3@NC‖AC full-cell

To investigate the practical feasibility of V_5S_8/Sb_2S_3@NC in full batteries, we created a PIB full-cell, as shown in Fig. S25a, where consist of V_5S_8/Sb_2S_3@NC anode and AC cathode (obtained *via* PTCDA annealing at 600 °C). At 0.1 A g^{-1} current density, Fig. S25b illustrates semi-plateau charge–discharge profiles. Additionally, cycling performance tests indicate a maintained discharge capacity exceeding 98 mA h g^{-1} even after 150 cycles, operating within 0.5–3.2 V under the same current condition (Fig. S26). The CE demonstrated a notable upward trend. The reactivation of V_5S_8/Sb_2S_3@NC may account for the structural changes that enhanced its electrochemical performance.

4. Conclusions

As anodes for PIBs, a rationally engineered V_5S_8/Sb_2S_3 encapsulated in N-doped carbon has been created. The presence of internal V_5S_8 nanoplates, interlayer Sb_2S_3 nanoribbons, and external N-doped carbon collectively contributes to a synergistic interaction within the V_5S_8/Sb_2S_3@NC structure. This integrated architecture promotes efficient electrolyte penetration and rapid ion diffusion, while simultaneously buffering volume fluctuations during repeated charge–discharge cycles. In addition, the *ex situ* XRD technology and HRTEM analysis were also used to explore V_5S_8/Sb_2S_3@NC storage processes. According to the DFT calculations, V_5S_8 and Sb_2S_3 display a significant disparity in Fermi energy levels, resulting in the production of an IEF across the heterointerface. This IEF drives electron migration from V_5S_8 to Sb_2S_3. The V_5S_8/Sb_2S_3@NC material demonstrates remarkable cycling durability, maintaining 301.5 mA h g^{-1} at the high current density of 1 A g^{-1} even across 600 cycles, with only 0.03% capacity fading each cycle. Furthermore, it delivers a significant reversible capacity of around 485 mA h g^{-1} afterwards 100 cycles at 0.1 A g^{-1}. Additionally, the V_5S_8/Sb_2S_3@NC anode and AC cathode of the potassium-ion full cell delivered a high capacity around 98 mA h g^{-1} at 0.1 A g^{-1}, maintaining this performance even after 150 cycles. Employing a general synthetic strategy to construct ultrathin-layered bimetallic sulfide heterostructures could provide valuable guidance for designing advanced electrode materials for PIBs.

Author contributions

Yulian Dong: conceptualization, data curation, investigation, methodology, visualization, formal analysis, writing – original draft; Yubin Fu: formal analysis, investigation, software; Vincent Hartmann: investigation, methodology, data curation; Changfan Xu: formal analysis, visualization; Ping Hong: data curation; Yueliang Li: data curation, formal analysis; Huaping Zhao: methodology, writing – review & editing. Weidong Shi: project administration, resources, supervision; Ute Kaiser: project administration, resources, supervision; Yong Lei: conceptualization, funding acquisition, methodology, project administration, resources, supervision, validation, writing – review & editing.

Conflicts of interest

There are no conflicts to declare.

Data availability

The data supporting this article have been included as part of the supplementary information (SI). Supplementary information: sample characterization, electrochemical measurements, theoretical calculation, video, and further experimental details. See DOI: **https://doi.org/10.1039/d6qi00253f**.

Acknowledgements

The authors acknowledge support from the Sino-German Centre for Research Promotion (GZ1579) and German Research Foundation (DFG, Project number 501766751). Yulian Dong appreciates the Postdoctoral Fellowship for Women Scientists start-up funding.

References

1 E. McCalla and S. Jia, Topology to improve battery technology, *Nat. Sustain.*, 2022, **5**, 181–182.

2 C. Xu, J. Qiu, Y. Dong, Y. Li, Y. Shen, H. Zhao, U. Kaiser, G. Shao and Y. Lei, Dual-Functional Electrode Promoting Dendrite-Free and CO_2 Utilization Enabled High-Reversible Symmetric Na-CO_2 Batteries, *Energy Environ. Mater.*, 2024, **7**, e12626.

3 W. Zhang, Y. Liu and Z. Guo, Approaching high-performance potassium-ion batteries via advanced design strategies and engineering, *Sci. Adv.*, 2019, **5**, eaav7412.

4 Y. Xu, C. Zhang, M. Zhou, Q. Fu, C. Zhao, M. Wu and Y. Lei, Highly nitrogen doped carbon nanofibers with superior rate capability and cyclability for potassium ion batteries, *Nat. Commun.*, 2018, **9**, 1720.

5 C. Zhang, Y. Xu, M. Zhou, L. Liang, H. Dong, M. Wu, Y. Yang and Y. Lei, Potassium Prussian Blue Nanoparticles: A Low-Cost Cathode Material for Potassium-Ion Batteries, *Adv. Funct. Mater.*, 2017, **27**, 1604307.

6 Y. Wu, J. Zheng, Y. Tong, X. Liu, Y. Sun, L. Niu and H. Li, Carbon Hollow Tube-Confined Sb/Sb_2S_3 Nanorod Fragments as Highly Stable Anodes for Potassium-Ion Batteries, *ACS Appl. Mater. Interfaces*, 2021, **13**, 51066–51077.

7 Y. Cheng, Z. Yao, Q. Zhang, J. Chen, W. Ye, S. Zhou, H. Liu and M.-S. Wang, In Situ Atomic-Scale Observation of Reversible Potassium Storage in Sb_2S_3@Carbon Nanowire Anodes, *Adv. Funct. Mater.*, 2020, **30**, 2005417.

8 H. Liu, Y. He, K. Cao, S. Wang, Y. Jiang, X. Liu, K.-J. Huang, Q.-S. Jing and L. Jiao, Stimulating the Reversibility of Sb_2S_3 Anode for High-Performance Potassium-Ion Batteries, *Small*, 2021, **17**, 2008133.

9 L. Cao, X. Gao, B. Zhang, X. Ou, J. Zhang and W.-B. Luo, Bimetallic Sulfide Sb_2S_3@FeS_2 Hollow Nanorods as High-Performance Anode Materials for Sodium-Ion Batteries, *ACS Nano*, 2020, **14**, 3610–3620.

10 S. Yao, J. Cui, Z. Lu, Z.-L. Xu, L. Qin, J. Huang, Z. Sadighi, F. Ciucci and J.-K. Kim, Unveiling the Unique Phase Transformation Behavior and Sodiation Kinetics of 1D van der Waals Sb_2S_3 Anodes for Sodium Ion Batteries, *Adv. Energy Mater.*, 2017, **7**, 1602149.

11 L. Li, W. Zhang, X. Wang, S. Zhang, Y. Liu, M. Li, G. Zhu, Y. Zheng, Q. Zhang, T. Zhou, W. K. Pang, W. Luo, Z. Guo and J. Yang, Hollow-Carbon-Templated Few-Layered V_5S_8 Nanosheets Enabling Ultrafast Potassium Storage and Long-Term Cycling, *ACS Nano*, 2019, **13**, 7939–7948.

12 T. Taniguchi, S. Li, L. Nurdiwijayanto, Y. Kobayashi, T. Saito, Y. Miyata, S. Obata, K. Saiki, H. Yokoi, K. Watanabe, T. Taniguchi, K. Tsukagoshi, Y. Ebina, T. Sasaki and M. Osada, Tunable Chemical Coupling in Two-Dimensional van der Waals Electrostatic Heterostructures, *ACS Nano*, 2019, **13**, 11214–11223.

13 T. Wang, M. Li, L. Yao, W. Yang and Y. Li, Controlled Growth Lateral/Vertical Heterostructure Interface for Lithium Storage, *Adv. Mater.*, 2024, **36**, 2402961.

14 J. Wang, B. Wang and B. Lu, Nature of Novel 2D van der Waals Heterostructures for Superior Potassium Ion Batteries, *Adv. Energy Mater.*, 2020, **10**, 2000884.

15 J. Li, H. Yang, J. Wu, S. Sun, T. Zhai and H. Xia, Harnessing the Defects at Hetero-Interface of Transition Metal Compounds for Advanced Charge Storage: A Review, *Small Struct.*, 2022, **3**, 2200022.

16 W. Wu, Y. Wang, S. Song, Z. Ge, C. Zhang, J. Huang, G. Xu, N. Wang, Y. Lu, Z. Deng, H. Duan, M. Liu and C. Tang, Built-In Electric Field in Freestanding Hydroxide/Sulfide Heterostructures for Industrially Relevant Oxygen Evolution, *Angew. Chem., Int. Ed.*, 2025, **64**, e202504972.

17 J. Hu, B. Li, X. Li, T. Yang, X. Yang, J. Qu, Y. Cai, H. Yang and Z. Lin, Lattice Match-Enabled Covalent Heterointerfaces with Built-in Electric Field for Efficient Hydrogen Peroxide Photosynthesis, *Adv. Mater.*, 2024, **36**, 2412070.

18 Z. Li, Z. Zhao, S. Pan, Y. Wang, S. Chi, X. Yi, J. Han, D. Kong, J. Xiao, W. Wei, S. Wu and Q.-H. Yang, Covalent Coating of Micro-Sized Silicon with Dynamically Bonded Graphene Layers Toward Stably Cycled Lithium Storage, *Adv. Energy Mater.*, 2023, **13**, 2300874.

19 Y. Dong, C. Yan, H. Zhao and Y. Lei, Recent Advances in 2D Heterostructures as Advanced Electrode Materials for Potassium-Ion Batteries, *Small Struct.*, 2022, **3**, 2100221.

20 J. Xu, H. Li, Y. Jin, D. Zhou, B. Sun, M. Armand and G. Wang, Understanding the Electrical Mechanisms in Aqueous Zinc Metal Batteries: From Electrostatic Interactions to Electric Field Regulation, *Adv. Mater.*, 2024, **36**, 2309726.

21 X. Yue, J. Fan and Q. Xiang, Internal Electric Field on Steering Charge Migration: Modulations, Determinations and Energy-Related Applications, *Adv. Funct. Mater.*, 2022, **32**, 2110258.

22 Y. Liu, Z. Tai, J. Zhang, W. K. Pang, Q. Zhang, H. Feng, K. Konstantinov, Z. Guo and H. K. Liu, Boosting potassium-ion batteries by few-layered composite anodes prepared via solution-triggered one-step shear exfoliation, *Nat. Commun.*, 2018, **9**, 3645.

23 C. Yang, X. Ou, X. Xiong, F. Zheng, R. Hu, Y. Chen, M. Liu and K. Huang, V_5S_8–graphite hybrid nanosheets as a high rate-capacity and stable anode material for sodium-ion batteries, *Energy Environ. Sci.*, 2017, **10**(1), 107–113.

24 L. Tang, P. Li, R. Cui, T. Peng, H.-X. Wei, Z. Wang, H. Wang, C. Yan, J. Mao, K. Dai, H. Chen, X. Zhang and J. Zheng, Adjusting Crystal Orientation to Promote Sodium-Ion Transport in V_5S_8@Graphene Anode Materials for High-Performance Sodium-Ion Batteries, *Small Methods*, 2023, **7**, 2201387.

25 Y. Zhang, S. Li, L. Liu, Y. Lin, S. Jiang, Y. Li, X. Ren, P. Zhang, L. Sun and H. Y. Yang, Double-Enhanced Core–Shell–Shell Sb_2S_3/Sb@TiO_2@C Nanorod Composites for Lithium- and Sodium-Ion Batteries, *ACS Appl. Mater. Interfaces*, 2022, **14**, 33064–33075.

26 W. Li, J. Li, T. Ma, G. Liao, F. Gao, W. Duan, K. Luo and C. Wang, Construction of Core–shell Sb_2S_3@Cds Nanorod

with Enhanced Heterointerface Interaction for Chromium-Containing Wastewater Treatment, *Small*, 2023, **19**, 2302737.

27 Y. Dong, C. Xu, Y. Li, C. Zhang, H. Zhao, U. Kaiser and Y. Lei, Ultrahigh-Rate and Ultralong-Duration Sodium Storage Enabled by Sodiation-Driven Reconfiguration, *Adv. Energy Mater.*, 2023, **13**, 2204324.

28 X. Li, H. Liang, X. Liu, R. Sun, Z. Qin, H. Fan and Y. Zhang, Ion-exchange strategy of CoS_2/Sb_2S_3 hetero-structured nanocrystals encapsulated into 3D interpenetrating dual-carbon framework for high-performance Na^+/K^+ batteries, *Chem. Eng. J.*, 2021, **425**, 130657.

29 T. Zhang, Y. Liu, J. Yu, Q. Ye, L. Yang, Y. Li and H. J. Fan, Biaxially Strained MoS_2 Nanoshells with Controllable Layers Boost Alkaline Hydrogen Evolution, *Adv. Mater.*, 2022, **34**, 2202195.

30 Y. Zhang, S. Yu, G. Lou, Y. Shen, H. Chen, Z. Shen, S. Zhao, J. Zhang, S. Chai and Q. Zou, Review of macroporous materials as electrochemical supercapacitor electrodes, *J. Mater. Sci.*, 2017, **52**, 11201–11228.

31 Y. Zhang, S. Li, L. Cheng, Y. Li, X. Ren, P. Zhang, L. Sun and H. Yang, Confining Sb_2 Se_3 nanorod yolk in a mesoporous carbon shell with an in-built buffer space for stable Li-ion batteries, *J. Mater. Chem. A*, 2021, **9**, 3388–3397.

32 P. Veselá and V. Slovák, N-doped carbon xerogels prepared by ammonia assisted pyrolysis: Surface characterisation, thermal properties and adsorption ability for heavy metal ions, *J. Anal. Appl. Pyrolysis*, 2014, **109**, 266–271.

33 S. Yousef, J. Eimontas, N. Striūgas and M. A. Abdelnaby, Influence of carbon black filler on pyrolysis kinetic behaviour and TG-FTIR-GC–MS analysis of glass fibre reinforced polymer composites, *Energy*, 2021, **233**, 121167.

34 L. P. Bakos, J. Mensah, K. László, T. Igricz and I. M. Szilágyi, Preparation and characterization of a nitrogen-doped mesoporous carbon aerogel and its polymer precursor, *J. Therm. Anal. Calorim.*, 2018, **134**, 933–939.

35 J. Dai, F. Zhu, B. Murugesan, Q. Zhang, X. Zhou, W. Ni and Y. Cai, Synergistic V_5S_8/CoS nanoparticles-embedded carbon nanofiber as binder-free flexible anode for sodium-ion batteries, *Ionics*, 2024, **30**, 217–227.

36 Ž. Živković, N. Štrbac, D. Živković, D. Grujičić and B. Boyanov, Kinetics and mechanism of Sb_2S_3 oxidation process, *Thermochim. Acta*, 2002, **383**, 137–143.

37 H. Zhang, H. Xu, Z. Xiao, G. Dong, Y. Cheng, F. Fei, X. Hu, L. Xu and L. Mai, Nanowires for Solid-State Lithium Batteries, *Adv. Funct. Mater.*, 2025, **35**, 2412548.

38 W. Kaidan, Y. Feng, S. Wu, J. Zhang, D. Xiong, L. Chen, Z. Feng, K. Wen and M. He, 3d Fluorine-Doped Carbon@Ti_3c_2 Mxene as Anode Material for High Performance Potassium Ion Batteries, *Soc. Sci. Res. Network*, 2022, 4104083, DOI: 10.2139/ssrn.4104083, preprint.

39 Y. Gu, Y. Pei, M. Zhao, C. Yang and Q. Jiang, Sn-, Sb- and Bi-Based Anodes for Potassium Ion Battery, *Chem. Rec.*, 2022, **22**, e202200098.

40 L. Shen, Y. Wang, F. Wu, I. Moudrakovski, P. A. van Aken, J. Maier and Y. Yu, Hierarchical Metal Sulfide/Carbon Spheres: A Generalized Synthesis and High Sodium-Storage Performance, *Angew. Chem., Int. Ed.*, 2019, **58**, 7238–7243.

41 B.-T. Liu, X.-M. Shi, X.-Y. Lang, L. Gu, Z. Wen, M. Zhao and Q. Jiang, Extraordinary pseudocapacitive energy storage triggered by phase transformation in hierarchical vanadium oxides, *Nat. Commun.*, 2018, **9**, 1375.

42 Y. Liu, Z. Sun, X. Sun, Y. Lin, K. Tan, J. Sun, L. Liang, L. Hou and C. Yuan, Construction of Hierarchical Nanotubes Assembled from Ultrathin V_3S_4@C Nanosheets towards Alkali-Ion Batteries with Ion-Dependent Electrochemical Mechanisms, *Angew. Chem., Int. Ed.*, 2020, **59**, 2473–2482.

43 C. Zhang, F. Han, F. Wang, Q. Liu, D. Zhou, F. Zhang, S. Xu, C. Fan, X. Li and J. Liu, Improving compactness and reaction kinetics of MoS_2@C anodes by introducing Fe_9S_{10} core for superior volumetric sodium/potassium storage, *Energy Storage Mater.*, 2020, **24**, 208–219.

44 L. Cao, B. Luo, B. Xu, J. Zhang, C. Wang, Z. Xiao, S. Li, Y. Li, B. Zhang, G. Zou, H. Hou, X. Ou and X. Ji, Stabilizing Intermediate Phases via Efficient Entrapment Effects of Layered VS_4/SnS@C Heterostructure for Ultralong Lifespan Potassium-Ion Batteries, *Adv. Funct. Mater.*, 2021, **31**, 2103802.

45 H. Huang, J. Cui, G. Liu, R. Bi and L. Zhang, Carbon-Coated $MoSe_2$/MXene Hybrid Nanosheets for Superior Potassium Storage, *ACS Nano*, 2019, **13**, 3448–3456.

46 Q. Pan, Z. Tong, Y. Su, Y. Zheng, L. Shang and Y. Tang, Flat–Zigzag Interface Design of Chalcogenide Heterostructure toward Ultralow Volume Expansion for High-Performance Potassium Storage, *Adv. Mater.*, 2022, **34**, 2203485.

47 Y. Cao, H. Chen, Y. Shen, M. Chen, Y. Zhang, L. Zhang, Q. Wang, S. Guo and H. Yang, SnS_2 Nanosheets Anchored on Nitrogen and Sulfur Co-Doped MXene Sheets for High-Performance Potassium-Ion Batteries, *ACS Appl. Mater. Interfaces*, 2021, **13**, 17668–17676.

48 S. Liu, H. Zhang, M. Zhou, X. Chen, Y. Sun and Y. Zhang, V_5S_8 nanoparticles anchored on carbon nanofibers for fast and durable sodium and potassium ion storage, *J. Electroanal. Chem.*, 2021, **903**, 115841.

49 L. Xu, X. Chen, W. Guo, L. Zeng, T. Yang, P. Xiong, Q. Chen, J. Zhang, M. Wei and Q. Qian, Co-construction of sulfur vacancies and carbon confinement in V_5S_8/CNFs to induce an ultra-stable performance for half/full sodium-ion and potassium-ion batteries, *Nanoscale*, 2021, **13**, 5033–5044.

50 J. Chen, Z. Tang, Z. Pan, W. Shi, Y. Wang, Z. Q. Tian and P. K. Shen, Template-free growth of spherical vanadium disulfide nanoflowers as efficient anodes for sodium/potassium ion batteries, *Mater. Des.*, 2020, **192**, 108780.

51 S. Chong, S. Qiao, X. Wei, T. Li, L. Yuan, S. Dong and W. Huang, Sb2S3-based conversion-alloying dual mechanism anode for potassium-ion batteries, *iScience*, 2021, **24**, 103494.

52 L. Cao, B. Zhang, H. Xia, C. Wang, B. Luo, X. Fan, J. Zhang and X. Ou, Hierarchical chrysanthemum-like MoS2/Sb heterostructure encapsulated into N-doped graphene framework for superior potassium-ion storage, *Chem. Eng. J.*, 2020, **387**, 124060.

53 H. Sun, G. Xin, T. Hu, M. Yu, D. Shao, X. Sun and J. Lian, High-rate lithiation-induced reactivation of mesoporous hollow spheres for long-lived lithium-ion batteries, *Nat. Commun.*, 2014, **5**, 4526.

54 B. E. Conway, V. Birss and J. Wojtowicz, The role and utilization of pseudocapacitance for energy storage by supercapacitors, *J. Power Sources*, 1997, **66**, 1–14.

55 J. Lu, H. Tong, S. Chen, C. Wang, X. Zeng, J. Tu and Q. Chen, One-Step Construction of V_5S_8 Nanoparticles Embedded in Amorphous Carbon Nanorods for High-Capacity and Long-Life Potassium Ion Half/Full Batteries, *ACS Appl. Mater. Interfaces*, 2021, **13**, 54308–54314.

56 S. Wang, P. Xiong, X. Guo, J. Zhang, X. Gao, F. Zhang, X. Tang, P. H. L. Notten and G. Wang, A Stable Conversion and Alloying Anode for Potassium-Ion Batteries: A Combined Strategy of Encapsulation and Confinement, *Adv. Funct. Mater.*, 2020, **30**, 2001588.

57 A. Radzwan, R. Ahmed, A. Shaari, A. Lawal and Y. Ng, First-principles calculations of antimony sulphide Sb_2S_3, *Malays. J. Fundam. Appl. Sci.*, 2017, **13**, 285–289.

58 H. Wang, D. Zhai and F. Kang, Solid electrolyte interphase (SEI) in potassium ion batteries, *Energy Environ. Sci.*, 2020, **13**, 4583–4608.

59 Y. Han, A. Vijaya Kumar Saroja, H. Tinker and Y. Xu, Interphases in the electrodes of potassium ion batteries, *JPhys Mater.*, 2022, **5**, 022001.

60 J. Wen, H. Fu, C. Gao, J. Zhou, A. M. Rao, S. Wen and B. Lu, Synergy Between Weak Solvent and Solid Electrolyte Interphase Enables High-Rate and Temperature-Resilient Potassium Ion Batteries, *Angew. Chem., Int. Ed.*, 2025, **64**, e202501155.

61 Z. Wang and S. Wang, Constructing built-in electric field to accelerate the asymmetric local charge distribution for efficient alkaline overall water/seawater splitting, *Appl. Catal., B*, 2024, **352**, 124002.

62 Y. Li, J. Zhang, Q. Chen, X. Xia and M. Chen, Emerging of Heterostructure Materials in Energy Storage: A Review, *Adv. Mater.*, 2021, **33**, 2100855.

63 G. Kresse and J. Furthmüller, Efficiency of *ab initio* total energy calculations for metals and semiconductors using a plane-wave basis set, *Comput. Mater. Sci.*, 1996, **6**, 15–50.

64 C. He, J. H. Zhang, W. X. Zhang and T. T. Li, GeSe/BP van der Waals Heterostructures as Promising Anode Materials for Potassium-Ion Batteries, *J. Phys. Chem. C*, 2019, **123**, 5157–5163.

65 B. Özdogru, Y. Cha, B. Gwalani, V. Murugesan, M. Song and Ö. Çapraz, In Situ Probing Potassium-Ion Intercalation-Induced Amorphization in Crystalline Iron Phosphate Cathode Materials, *Nano Lett.*, 2026, **21**(18), 7579–7586.

66 J. Ding, D. Ji, Y. Yue and M. M. Smedskjaer, Amorphous Materials for Lithium-Ion and Post-Lithium-Ion Batteries, *Small*, 2024, **20**, 2304270.

67 T. Guo, P. Hu, L. Li, Z. Wang and L. Guo, Amorphous materials emerging as prospective electrodes for electrochemical energy storage and conversion, *Chem*, 2023, **9**, 1080–1093.